REPORT

BIOMEDICINE

Multivascular networks and functional intravascular topologies within biocompatible hydrogels

Bagrat Grigoryan[1]*, Samantha J. Paulsen[1]*, Daniel C. Corbett[2,3]*, Daniel W. Sazer[1], Chelsea L. Fortin[3,4], Alexander J. Zaita[1], Paul T. Greenfield[1], Nicholas J. Calafat[1], John P. Gounley[5]†, Anderson H. Ta[1], Fredrik Johansson[2,3], Amanda Randles[5], Jessica E. Rosenkrantz[6], Jesse D. Louis-Rosenberg[6], Peter A. Galie[7], Kelly R. Stevens[2,3,4]‡, Jordan S. Miller[1]‡

Solid organs transport fluids through distinct vascular networks that are biophysically and biochemically entangled, creating complex three-dimensional (3D) transport regimes that have remained difficult to produce and study. We establish intravascular and multivascular design freedoms with photopolymerizable hydrogels by using food dye additives as biocompatible yet potent photoabsorbers for projection stereolithography. We demonstrate monolithic transparent hydrogels, produced in minutes, comprising efficient intravascular 3D fluid mixers and functional bicuspid valves. We further elaborate entangled vascular networks from space-filling mathematical topologies and explore the oxygenation and flow of human red blood cells during tidal ventilation and distension of a proximate airway. In addition, we deploy structured biodegradable hydrogel carriers in a rodent model of chronic liver injury to highlight the potential translational utility of this materials innovation.

The morphologies of the circulatory and pulmonary systems are physically and evolutionarily entangled (*1*). In air-breathing vertebrates, these bounded and conserved vessel topologies interact to enable the oxygen-dependent respiration of the entire organism (*2*–*4*). To build and interrogate soft hydrogels containing such prescribed biomimetic and multivascular architectures, we sought to use stereolithography (fig. S1) (*5*), commonly employed to efficiently convert photoactive liquid resins into structured plastic parts through localized photopolymerization (*6*, *7*). Compared with extrusion 3D printing, which deposits voxels in a serial fashion (*8*–*12*), photocrosslinking can be highly parallelized via image projection to simultaneously and independently address millions of voxels per time step. In stereolithography, *xy* resolution is determined by the light path, whereas *z* resolution is dictated by light-attenuating additives that absorb excess light and confine the polymerization to the desired layer thickness, thereby improving pattern fidelity. In the absence of suitable photoabsorber additives, 3D photopatterning of soft hydrogels has been limited in the types of patterns that can be generated (*13*–*16*) or has required complex, expensive, and low-throughput microscopy to enhance *z* resolution via the multiphoton effect (*17*–*19*). However, common light-blocking chemicals used for photoresist patterning or plastic part fabrication, such as Sudan I, are not suitable for biomanufacturing owing to their known genotoxic and carcinogenic characteristics (*20*). Therefore, we hypothesized that the identification of nontoxic light blockers for projection stereolithography could provide a major advance to the architectural richness available for the design and generation of widely used biocompatible hydrogels.

Here, we establish that synthetic and natural food dyes, widely used in the food industry, can be applied as potent biocompatible photoabsorbers to enable the stereolithographic production of hydrogels containing intricate and functional vascular architectures. We identified candidate photoabsorbers among food additives whose absorbance spectra encompass visible light wavelengths that can be used for biocompatible photopolymerization. We initially sought to generate monolithic hydrogels, composed primarily of water and poly(ethylene glycol) diacrylate [PEGDA, 6 kDa, 20 weight % (wt %)], with a 1-mm cylindrical channel oriented perpendicular to the light-projection axis. The fabrication of even this trivial design cannot be easily realized because of the dilute nature of such aqueous formulations, in which the low mass fraction of crosslinkable groups and the requisite longer polymerization times result in inadvertent polymerization and solidification within the narrow void spaces that were designed to be hollow perfusable vasculature (figs. S2 to S4).

We determined that aqueous pre-hydrogel solutions containing tartrazine (yellow food coloring FD&C Yellow 5, E102), curcumin (from turmeric), or anthocyanin (from blueberries) can each yield hydrogels with a patent vessel (figs. S2 to S5). In addition to these organic molecules, inorganic gold nanoparticles (50 nm), widely regarded for their biocompatibility and light-attenuating properties (*21*), also function as an effective photoabsorbing additive to generate perfusable hydrogels (fig. S4).

To understand how these photoabsorbers affect the gelation kinetics of photopolymerizable hydrogels, we performed photorheological characterization with short-duration light exposures, which indicate that these additives cause a dose-dependent delay in the induction of photocrosslinking (figs. S2D and S4E). Saturating light exposures that extend beyond the reaction termination point demonstrate that suitable additives did not ultimately interfere with the reaction because hydrogels eventually reached an equivalent storage modulus independent of the additive concentration (figs. S2D and S4E). We selected tartrazine as a photoabsorber for further studies. In addition to its low toxicity in humans and broad utility in the food industry (*22*), we observed that this hydrophilic dye is easily washed out of generated hydrogels (70% elutes within 3 hours for small gels), resulting in nearly transparent constructs suitable for imaging (fig. S2E). Some tartrazine may also be degraded during polymerization, as tartrazine is known to be sensitive to free radicals (*23*). Submerging gels in water or saline solution to remove soluble tartrazine also flushes the vascular topology and removes unreacted pre-hydrogel solution. In contrast to tartrazine, curcumin is lipophilic and does not wash out in aqueous solutions; anthocyanin has a peak absorbance far from our intended 405-nm light source, requiring high concentrations for suitable potency; and gold nanoparticles are physically entrapped and make transmission or fluorescence microscopy impractical (fig. S4E).

We assessed whether this materials insight could similarly impart new architectural freedoms to more-advanced photoactive materials. Photoabsorber additives are necessary and sufficient to enable vessel construction in thiol-ene step-growth photopolymerization (*24*) of hydrogels and in a continuous liquid interface production (*6*) workflow for the generation of hydrogels (fig. S5). We observed strong lamination between adjacent fabricated layers and a rapid response of the patterned hydrogel to mechanical deformations (fig. S6). This facile generation of soft hydrogels with patent cylindrical vessels oriented orthogonal to the light-projection axis suggests an extensive design flexibility toward the generation of complex vascular topologies, and

[1]Department of Bioengineering, Rice University, Houston, TX 77005, USA. [2]Department of Bioengineering, University of Washington, Seattle, WA 98195, USA. [3]Institute for Stem Cell and Regenerative Medicine, University of Washington, Seattle, WA 98195, USA. [4]Department of Pathology, University of Washington, Seattle, WA 98195, USA. [5]Department of Biomedical Engineering, Duke University, Durham, NC 27708, USA. [6]Nervous System, Somerville, MA 02143, USA. [7]Department of Biomedical Engineering, Rowan University, Glassboro, NJ 08028, USA.
*These authors contributed equally to this work. †Present address: Computational Science and Engineering Division, Oak Ridge National Laboratory, Oak Ridge, TN 37830, USA.
‡Corresponding author. Email: ksteve@uw.edu (K.R.S.); jmil@rice.edu (J.S.M.)

the optical clarity of resultant hydrogels implies imaging methodologies suitable for characterization and validation of fluid flows.

Next, we investigated the ability to form hydrogels containing functional intravascular topologies. We first explored chaotic mixers: intravascular topologies that homogenize fluids as a result of interactions between fluid flow streams and the vessel geometry (*25*, *26*). Whereas macroscale static mixers have found broad utility in industrial processes (*27*) because of their unparalleled efficiency, translation of intravascular static mixers into microfluidic systems has been difficult to implement, owing to their complex 3D topology. To this end, we generated monolithic hydrogels with an integrated static mixer composed of 3D twisted-fin elements (150 μm thick) of alternating chirality inside a 1-mm cylindrical channel. We applied laminar fluid streams to the static mixer at a low Reynolds number (0.002) and observed rapid mixing per unit length (Fig. 1A) and as a function of fin number (fig. S7). The elasticity and compliance of PEG-based hydrogels (fig. S6) enabled the facile generation of a 3D functional bicuspid venous valve (Fig. 1B). We observed that the valve leaflets are dynamic, respond rapidly to pulsatile anterograde and retrograde flows, and promote the formation of stable mirror image vortices in the valve sinuses (Fig. 1B and movie S1) according to established mappings of native tissue (*28*, *29*).

Solid organs contain distinct fluid networks that are physically and chemically entangled, providing the rich extracellular milieu that is a hallmark of multicellular life. The ability to fabricate such multivascular topologies within biocompatible and aqueous environments could enable a step change in the fields of biomaterials and tissue engineering. A first objective is the development of an efficient framework to design entangled networks that can provide suitable blueprints for their fabrication within hydrogels. Separate vascular networks must not make a direct fluid connection or they would topologically reduce to a single connected network. We find that mathematical space-filling and fractal topology algorithms provide an efficient parametric language to design complex vascular blueprints and a mathematical means to design a second vascular architecture that does not intersect the first (Fig. 2). We demonstrate a selection of hydrogels (20 wt %, 6-kDa PEGDA) containing entangled vascular networks based on 3D mathematical algorithms (Fig. 2, A to D): a helix surrounding an axial vessel, 1° and 2° Hilbert curves, a bicontinuous cubic lattice (based on a Schwarz P surface), and a torus entangled with a torus knot. Perfusion with colored dyes and micro-computed tomography (μCT) analysis demonstrate pattern fidelity, vascular patency, and

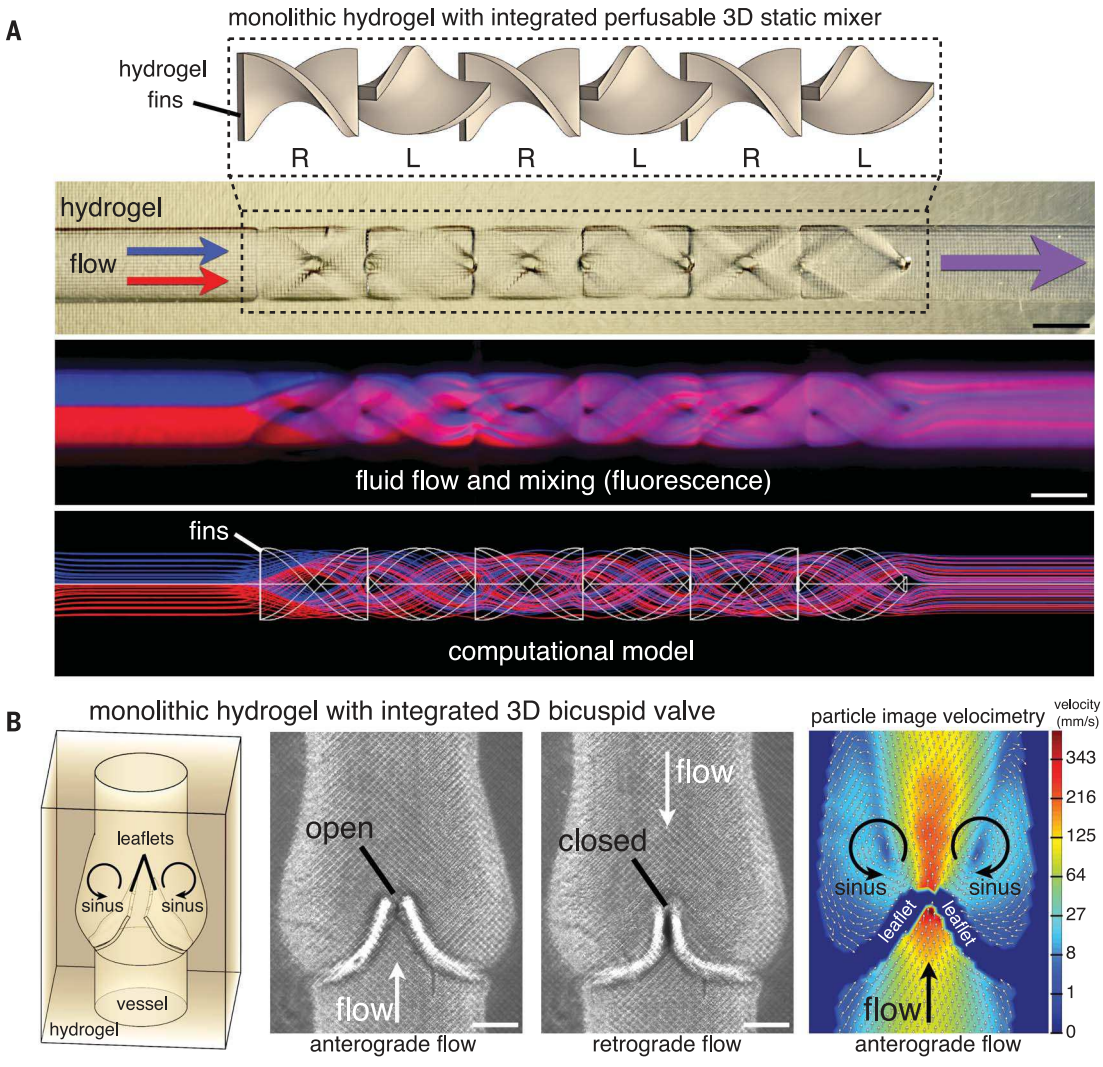

Fig. 1. Monolithic hydrogels with functional intravascular topologies. (**A**) Monolithic hydrogels with a perfusable channel containing integrated fin elements of alternating chirality. These static elements rapidly promote fluid dividing and mixing (as shown by fluorescence imaging), consistent with a computational model of flow (scale bars, 1 mm). (**B**) Hydrogels with a functional 3D bicuspid valve integrated into the vessel wall under anterograde and retrograde flows (scale bars, 500 μm). Particle image velocimetry demonstrates stable mirror image vortices in the sinus region behind open valve leaflets.

fluidic independence between the two networks (Fig. 2, A to D, and movie S2).

We sought to evaluate the efficiency of intervascular interstitial transport by measuring the delivery of oxygen from a source vessel to perfused human red blood cells (RBCs) flowing in an adjacent 3D topology. We tessellated the entangled helical topology shown in Fig. 2A along a serpentine path while maintaining the intervessel distance at 300 μm (Fig. 2E). Perfusion of deoxygenated RBCs [oxygen partial pressure (P_{O_2}) ≤ 40 mmHg; oxygen saturation (S_{O_2}) ≤ 45%] into the helical channel during ventilation of the serpentine channel with humidified gaseous oxygen (7 kPa) caused a noticeable color change of RBCs from dark red at the inlet to bright red at the outlet (Fig. 2, E and F). Collection of perfused RBCs showed significantly higher S_{O_2} and P_{O_2} relative to deoxygenated RBCs loaded at the inlet and negative control gels ventilated with humidified nitrogen gas (Fig. 2G and fig. S8).

Although this serpentine-helix design demonstrates the feasibility of intervascular oxygen transport between 3D entangled networks, we sought to introduce additional structural features of native distal lung into a bioinspired model of alveolar morphology and oxygen transport. In particular, the realization of 3D hydrogels that contain branching networks and that can support mechanical distension during cyclic ventilation of a pooled airway could enable investigations of the performance of lung morphologies derived from native structure (*30*) and could provide a complete workflow for the development and examination of new functional topologies. Over the past several decades, alveolar morphology has been approximated mathematically as 3D space-filling tessellations of polyhedra (*31*–*34*). However, the translation of these ideas into useful blueprints has remained nontrivial because of the need for efficient space-filling tessellations and an ensheathing vasculature that closely tracks the curvature of the 3D airway topography. Our solution is to calculate a 3D topological offset of the airway (moving each face in its local normal

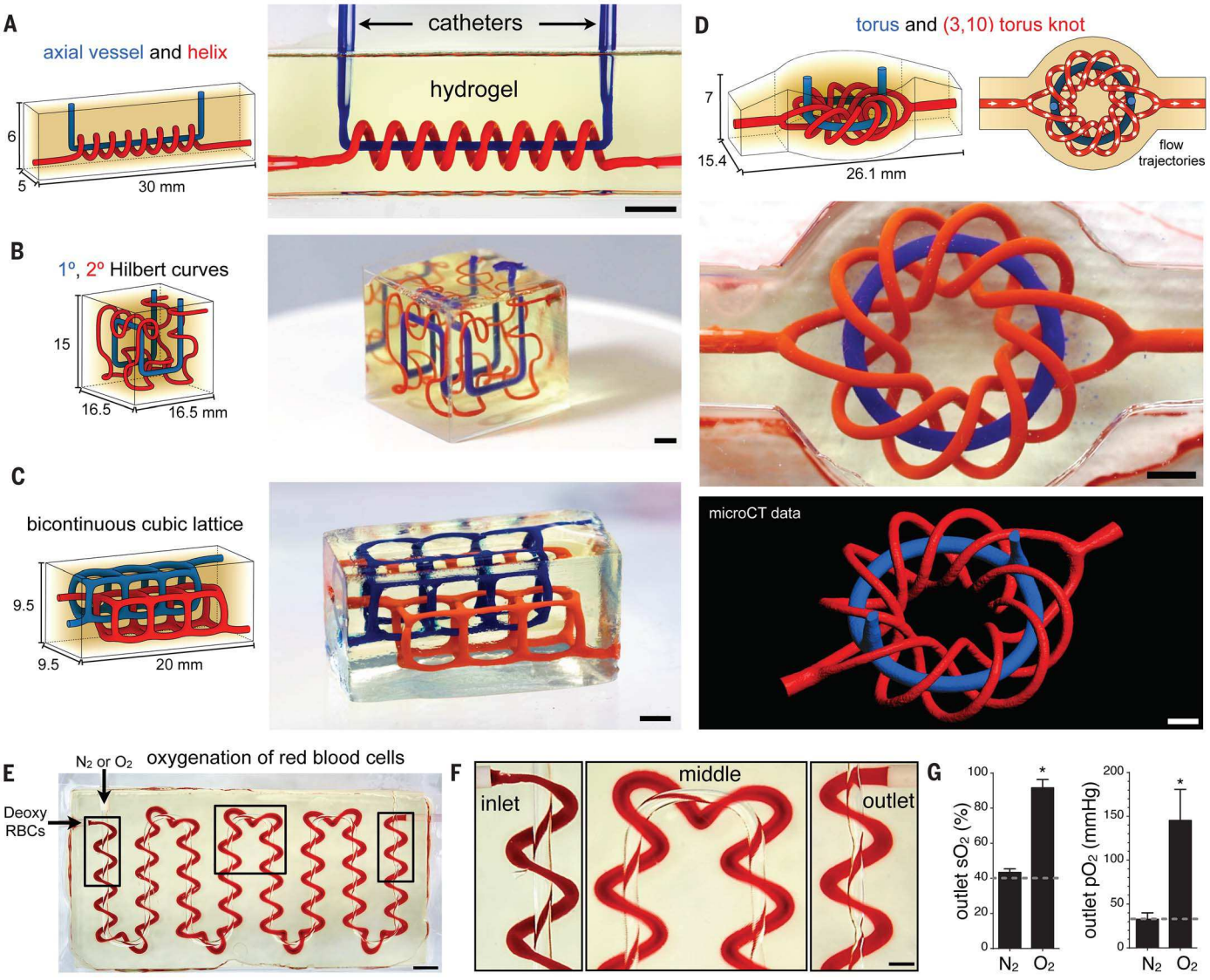

Fig. 2. Entangled vascular networks. (**A** to **D**) Adaptations of mathematical space-filling curves to entangled vessel topologies within hydrogels (20 wt % PEGDA, 6 kDa): (A) axial vessel and helix, (B) interpenetrating Hilbert curves, (C) bicontinuous cubic lattice, and (D) torus and (3,10) torus knot (scale bars, 3 mm). (**E**) Tessellation of the axial vessel and its encompassing helix along a serpentine pathway. The photograph is a top-down view of a fabricated hydrogel with oxygen and RBC delivery to respective vessels. During perfusion, RBCs change color from dark red (at the RBC inlet) to bright red (at the RBC outlet) (scale bar, 3 mm). Boxed regions are magnified in (**F**) (scale bar, 1 mm). (**G**) Perfused RBCs were collected at the outlet and quantified for S_{O_2} and P_{O_2}. Oxygen flow increased S_{O_2} and P_{O_2} of perfused RBCs compared with deoxygenated RBCs perfused at the inlet (dashed line) and a nitrogen flow negative control ($N \geq 3$ replicates, data are mean ± SD, $^*P < 2 \times 10^{-7}$ by Student's t test).

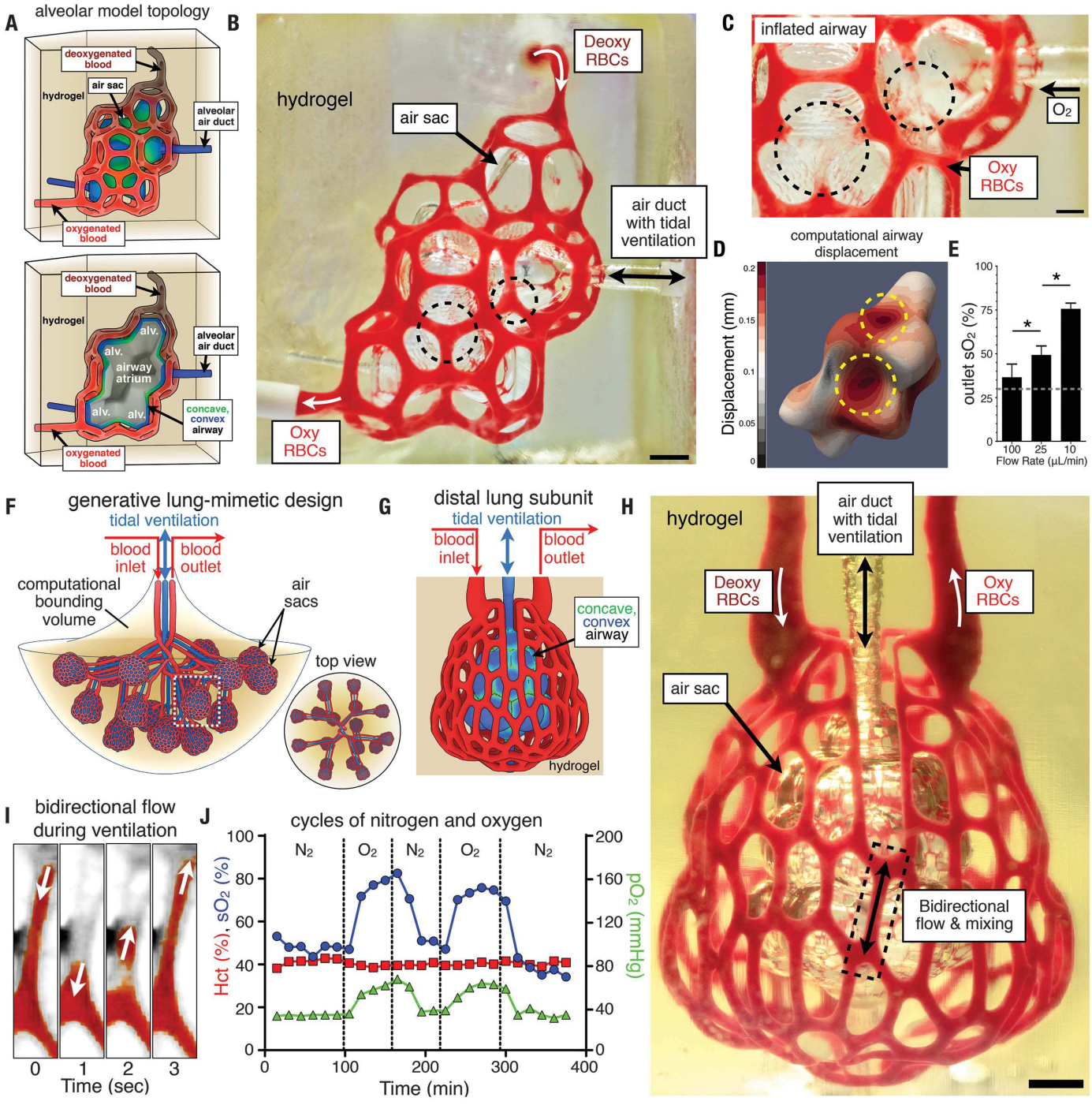

Fig. 3. Tidal ventilation and oxygenation in hydrogels with vascularized alveolar model topologies. (**A**) (Top) Architectural design of an alveolar model topology based on a Weaire-Phelan 3D tessellation and topologic offset to derive an ensheathing vasculature. (Bottom) Cutaway view illustrates the model alveoli (alv.) with a shared airway atrium. Convex (blue) and concave (green) regions of the airway are highlighted. (**B**) Photograph of a printed hydrogel during RBC perfusion while the air sac was ventilated with O_2 (scale bar, 1 mm). (**C**) Upon airway inflation with oxygen, concave regions of the airway (dashed black circles) squeeze adjacent blood vessels and cause RBC clearance (scale bar, 500 µm). (**D**) A computational model of airway inflation demonstrates increased displacement at concave regions (dashed yellow circles). (**E**) Oxygen saturation of RBCs increased with decreasing RBC flow rate ($N = 3$, data are mean ± SD, $^*P < 9 \times 10^{-4}$ by Student's t test). The dashed line indicates So_2 of deoxygenated RBCs perfused at the inlet. (**F**) Elaboration of a lung-mimetic design through generative growth of the airway, offset growth of opposing inlet and outlet vascular networks, and population of branch tips with a distal lung subunit. (**G**) The distal lung subunit is composed of a concave and convex airway ensheathed in vasculature by 3D offset and anisotropic Voronoi tessellation. (**H**) Photograph of a printed hydrogel containing the distal lung subunit during RBC perfusion while the air sac was ventilated with O_2 (scale bar, 1 mm). (**I**) Threshold view of the area enclosed by the dashed box in (H) demonstrates bidirectional RBC flow during ventilation. (**J**) Distal lung subunit can stably withstand ventilation for more than 10,000 cycles (24 kPa, 0.5 Hz) and demonstrates RBC sensitivity to ventilation gas (N_2 or O_2).

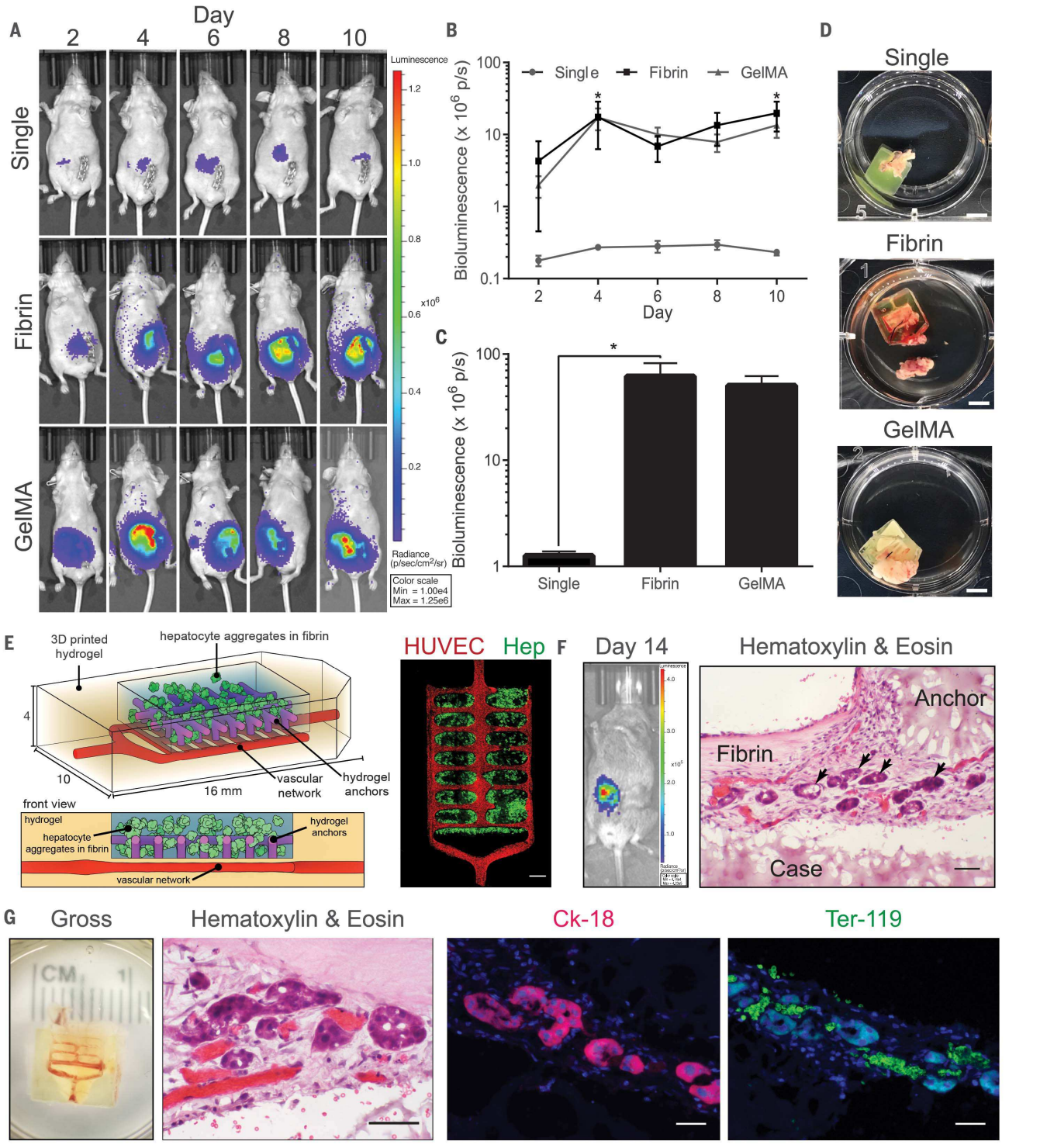

Fig. 4. Engraftment of functional hepatic hydrogel carriers. (**A** to **C**) Albumin promoter activity was enhanced in hydrogel carriers containing hepatic aggregates after implantation in nude mice. Data from all time points for each condition are shown in (B) [$N = 4$, $^*P < 0.05$ by two-way analysis of variance (ANOVA) followed by Tukey's post-hoc test]. Cumulative bioluminescence for each condition is shown in (C) ($N = 4$, $^*P < 0.05$ by one-way ANOVA followed by Tukey's post-hoc test). Error bars indicate SEM. GelMA, gelatin methacrylate. (**D**) Gross images of hydrogels upon resection (scale bars, 5 mm). (**E**) (Left) Prevascularized hepatic hydrogel carriers are created by seeding endothelial cells (HUVECs) in the vascular network after printing. (Right) Confocal microscopy observations show that hydrogel anchors physically entrap fibrin gel containing the hepatocyte aggregates (Hep) (scale bar, 1 mm). (**F**) Hepatocytes in prevascularized hepatic hydrogel carriers exhibit albumin promoter activity after implantation in mice with chronic liver injury. Graft sections stained with H&E show positioning of hepatic aggregates (black arrows) relative to printed (case, anchor) and nonprinted (fibrin) components of the carrier system (scale bar, 50 μm). (**G**) Hydrogel carriers are infiltrated with host blood (gross, H&E). Carriers contain aggregates that express the marker cytokeratin-18 (Ck-18) and are in close proximity to Ter-119–positive RBCs (scale bars, 40 μm).

direction) and have the new surface serve as the template on which a vascular skeleton is built. With this approach, we developed a bioinspired alveolar model with an ensheathing vasculature from 3D tessellations of the Weaire-Phelan foam topology (*35*) (Fig. 3 and fig. S9). Although the fundamental units of the Weaire-Phelan foam are convex polyhedra (fig. S9), 3D tessellations can produce a surface containing both convex and concave regions reminiscent of native alveolar air sacs (*30*) with a shared airway atrium supporting alveolar buds (Fig. 3A). We extended the manifold air surface in the normal direction, removed faces, and ensheathed edges in a smoothed polygonal mesh to form a highly branched vascular network (containing 185 vessel segments and 113 fluidic branch points) that encloses the airway and tracks its curvature (fig. S9B).

We printed hydrogels (20 wt %, 6-kDa PEGDA) patterned with the alveolar model topology at a voxel resolution of 5 pl and a print time of 1 hour (Fig. 3B). Cyclic ventilation of the pooled airway with humidified oxygen gas (10 kPa, 0.5 Hz) led to noticeable distension and an apparent change in the curvature of concave airway regions (fig. S9C). Perfusion of deoxygenated RBCs at the blood vessel inlet (10 to 100 μm/min) during cyclic ventilation led to observable compression and RBC clearance from vessels adjacent to concave airway regions (Fig. 3, B and C). By observing dilute RBC streams at the early stages of perfusion, we also discerned that the cyclic compression of RBC vessels—actuated by the concave airway regions upon each inflation cycle—acts as switching valves to redirect fluid streams to neighboring vessel segments (movie S3). We implemented a simplified 2D computational model of airway inflation (fig. S9D), which predicts anisotropic distension of the airway and compression of adjacent blood vessels, corresponding to local curvature (fig. S9E). In addition, analysis from a 3D computational model supports anisotropic distension of the concave regions of the airway during inflation (Fig. 3D). Despite the volume of the alveolar model hydrogel (0.8 ml) being <25% of that of the serpentine-helix model (3.5 ml), we measured similar oxygenation efficiencies for the two designs (Fig. 3E). Our data suggest that branching topology, hydrogel distension, and redirection of fluid streams during ventilation may boost intravascular mixing and allow faster volumetric uptake of oxygen by the well-mixed RBCs. Vascular constriction during breathing has been previously described as an important fluid control mechanism in the mammalian lung (*36*), and here we provide a means to actualize these ideas in completely defined and biocompatible materials and within aqueous environments.

To extend this work toward a coherent approximation of scalable lung-mimetic design, we must consolidate the location of the vascular inlet, vascular outlet, and air duct, such that distal lung subunits can be populated on the tips of multiscale branching architecture. Therefore, within a given computational bounding volume, we first derive a branching airway (Fig. 3F). Next, the centerlines of inlet and outlet blood vessel networks are grown 180° opposite each other across and topologically offset from the airway, and the blood vessels traverse down to the tips of all daughter branches. The final step is to populate the tips of each distal lung with an alveolar unit cell (Fig. 3G and movie S4) whose ensheathing vasculature (containing 354 vessel segments and 233 fluidic branch points) itself is an anisotropic Voronoi surface tessellation along a topological offset of its local airway (fig. S9, F and G). We found that hydrogels (20 wt %, 6-kDa PEGDA) could withstand more than 10,000 ventilation cycles (at 24 kPa and a frequency of 0.5 Hz) over 6 hours during RBC perfusion and while switching the inflow gas between humidified oxygen and humidified nitrogen (Fig. 3, H to J). Color-filtered views of the early stages of RBC perfusion (Fig. 3I) indicate that ventilation promotes RBC mixing and bidirectional flows within selected vessel segments near the midpoint of the distal lung subunit (movie S4).

We use our custom stereolithography apparatus for tissue engineering (SLATE) to demonstrate production of tissue constructs containing mammalian cells (figs. S1, S10, and S11 and movie S5). Lung-mimetic architectures can also be populated with human lung fibroblasts in the bulk of the interstitial space and human epithelial-like cells in the airway (fig. S12), which could facilitate the development of a hydrogel analog of a lab-on-a-chip lung design (*37*). Finally, we subjected primary human mesenchymal stem cells (hMSCs) to SLATE fabrication (with mixtures of PEGDA and gelatin methacrylate) and show that the cells within cylindrical fabricated hydrogels remain viable and can undergo osteogenic differentiation (fig. S13D). In related multiweek perfusion tissue culture of hMSCs with osteogenic differentiation media, osteogenic marker–positive hMSCs were visible throughout the gel (fig. S14). These studies indicate that SLATE fabrication supports rapid biomanufacturing, can maintain the viability of mammalian cell lines, supports the normal function and differentiation of primary human stem cells, and provides an experimentally tractable means to explore stem cell differentiation as a function of soluble factor delivery via vascular perfusion.

We next sought to establish the utility of this process for fabricating structurally complex and functional tissues for therapeutic transplantation. In particular, the liver is the largest solid organ in the human body, carrying out hundreds of essential tasks in a manner thought to be dependent on its structural topology. We created complex structural features in hydrogel within the expanded design space imparted by SLATE to assemble multimaterial liver tissues. Bioprinted single-cell tissues and bioprinted hydrogel carriers containing hepatocyte aggregates were fabricated (Fig. 4, A to C). The albumin promoter activity of tissue carriers loaded with aggregates was enhanced by more than a factor of 60 compared with that of implanted tissues containing single cells (Fig. 4, B and C). Furthermore, upon gross examination of tissues after resection, hydrogel carrier tissues appeared to have more integration with host tissue and blood (Fig. 4D). Despite the improved utility of hepatic aggregates over single cells, aggregate size puts substantial architectural limitations on 3D printing because aggregates are larger in size than our lowest voxel resolution (50 μm). To accommodate these design constraints, we built a more advanced carrier that can deliver hepatic aggregates within natural fibrin gel, has a vascular compartment that can be seeded with endothelial cells, and incorporates structural hydrogel anchors to physically, rather than chemically, retain the fibrin gel and facilitate remodeling between the graft and host tissue (Fig. 4E and fig. S15). Microchannel networks were seeded with human umbilical vein endothelial cells (HUVECs) because our previous studies demonstrated that inclusion of endothelial cords improved tissue engraftment (*38*). We then evaluated whether optimized bioengineered liver tissues would survive transplantation in a rodent model of chronic liver injury. After 14 days of engraftment in mice with chronic liver injury, hepatic hydrogel carriers exhibited albumin promoter activity indicative of surviving functional hepatocytes (Fig. 4F). Immunohistological characterization revealed the presence of hepatic aggregates adhered to printed hydrogel components that stained positively for the marker cytokeratin-18 (Fig. 4, F and G). Further characterization through gross examination and higher-magnification images of slides stained with hematoxylin and eosin (H&E) indicated the presence of host blood in explanted tissues. Immunostaining using a monoclonal antibody against Ter-119 confirmed the erythroid identity of cells in microvessels adjacent to hepatic microaggregates in explanted tissues (Fig. 4G, right). This work provides an approach to address long-standing design limitations in tissue engineering that have hindered progress of preclinical studies.

We have identified readily available food dyes that can serve as potent photoabsorbers for biocompatible and cytocompatible production of hydrogels containing functional vascular topologies for studies of fluid mixers, valves, intervascular transport, nutrient delivery, and host engraftment. With our stereolithographic process, there is potential for simultaneous and orthogonal control over tissue architecture and biomaterials for the design of regenerative tissues.

REFERENCES AND NOTES

1. R. Monahan-Earley, A. M. Dvorak, W. C. Aird, *J. Thromb. Haemost.* **11** (suppl. 1), 46–66 (2013).
2. G. R. Scott, *J. Exp. Biol.* **214**, 2455–2462 (2011).
3. E. R. Schachner, J. R. Hutchinson, C. Farmer, *PeerJ* **1**, e60 (2013).
4. C. G. Farmer, *Physiology* **30**, 260–272 (2015).
5. Supplementary figures, as well as materials and methods, are available as supplementary materials.
6. J. R. Tumbleston *et al.*, *Science* **347**, 1349–1352 (2015).
7. B. E. Kelly *et al.*, *Science* **363**, 1075–1079 (2019).
8. J. S. Miller *et al.*, *Nat. Mater.* **11**, 768–774 (2012).
9. T. J. Hinton *et al.*, *Sci. Adv.* **1**, e1500758 (2015).
10. T. Bhattacharjee *et al.*, *Sci. Adv.* **1**, e1500655 (2015).
11. D. B. Kolesky, K. A. Homan, M. A. Skylar-Scott, J. A. Lewis, *Proc. Natl. Acad. Sci. U.S.A.* **113**, 3179–3184 (2016).
12. H.-W. Kang *et al.*, *Nat. Biotechnol.* **34**, 312–319 (2016).

13. V. Liu Tsang *et al*., *FASEB J.* **21**, 790–801 (2007).
14. H. Lin *et al*., *Biomaterials* **34**, 331–339 (2013).
15. J. A. S. Neiman *et al*., *Biotechnol. Bioeng.* **112**, 777–787 (2015).
16. X. Ma *et al*., *Proc. Natl. Acad. Sci. U.S.A.* **113**, 2206–2211 (2016).
17. M. S. Hahn, J. S. Miller, J. L. West, *Adv. Mater.* **18**, 2679–2684 (2006).
18. C. A. DeForest, K. S. Anseth, *Nat. Chem.* **3**, 925–931 (2011).
19. K. A. Heintz *et al*., *Adv. Healthc. Mater.* **5**, 2153–2160 (2016).
20. T. M. Fonovich, *Drug Chem. Toxicol.* **36**, 343–352 (2013).
21. S. Kumar, J. Aaron, K. Sokolov, *Nat. Protoc.* **3**, 314–320 (2008).
22. L. J. Stevens, J. R. Burgess, M. A. Stochelski, T. Kuczek, *Clin. Pediatr.* **54**, 309–321 (2015).
23. M. Li *et al*., *J. Agric. Food Chem.* **62**, 12052–12060 (2014).
24. C. A. DeForest, B. D. Polizzotti, K. S. Anseth, *Nat. Mater.* **8**, 659–664 (2009).
25. A. D. Stroock *et al*., *Science* **295**, 647–651 (2002).
26. D. Therriault, S. R. White, J. A. Lewis, *Nat. Mater.* **2**, 265–271 (2003).
27. A. Ghanem, T. Lemenand, D. Della Valle, H. Peerhossaini, *Chem. Eng. Res. Des.* **92**, 205–228 (2014).
28. F. Lurie, R. L. Kistner, B. Eklof, D. Kessler, *J. Vasc. Surg.* **38**, 955–961 (2003).
29. E. Bazigou, T. Mäkinen, *Cell. Mol. Life Sci.* **70**, 1055–1066 (2013).
30. C. C. W. Hsia, D. M. Hyde, E. R. Weibel, *Compr. Physiol.* **6**, 827–895 (2016).
31. J. Mead, T. Takishima, D. Leith, *J. Appl. Physiol.* **28**, 596–608 (1970).
32. A. Linhartová, W. Caldwell, A. E. Anderson, *Anat. Rec.* **214**, 266–272 (1986).
33. Y. C. Fung, *J. Appl. Physiol.* **64**, 2132–2141 (1988).
34. P. Hofemeier, J. Sznitman, *J. Biomech. Eng.* **136**, 061007 (2014).
35. D. Weaire, R. Phelan, *Philos. Mag. Lett.* **69**, 107–110 (1994).
36. J. B. West, C. T. Dollery, A. Naimark, *J. Appl. Physiol.* **19**, 713–724 (1964).
37. D. Huh *et al*., *Science* **328**, 1662–1668 (2010).
38. K. R. Stevens *et al*., *Sci. Transl. Med.* **9**, eaah5505 (2017).
39. J. S. Miller, Dataset for: Multivascular networks and functional intravascular topologies within biocompatible hydrogels, Version 1.0, Zenodo (2019); https://doi.org/10.5281/zenodo.2614071
40. A. P. Randles, V. Kale, J. Hammond, W. Gropp, E. Kaxiras, in *Proceedings of the 2013 IEEE 27th International Symposium on Parallel and Distributed Processing* (IEEE, 2013), pp. 1063–1074.
41. L. Andrus *et al*., *Hepatology* **54**, 1901–1912 (2011).

ACKNOWLEDGMENTS

We thank the large number of open-source and related projects that facilitated this work, including Arduino.cc, RepRap.org, UltiMachine.com, Ultimaker.com, Blender.org, Python.org, ImageMagick.org, Git, NIH ImageJ, Fiji.sc, and the NIH 3D Print Exchange. We thank G. Calderon, P. Deme, S. Chen, A. Porter, H. Jackson, S. Panchavati, G. Quilap (Prime Camera), and F. Castaldi (Ikan) for technical assistance; T. J. Vadakkan and C.-W. Hsu from the Optical Imaging and Vital Microscopy Core at Baylor College of Medicine for assistance with μCT; A. J. Budi Utama, W. Hauser, and M. Guerra for assistance with the IVIS imaging system; and M. Dickinson, M. Wettergreen, J. Tabor, and S. Cutting for helpful discussions. **Funding:** This work was supported in part by the Robert J. Kleberg, Jr. and Helen C. Kleberg Foundation (J.S.M.), the U.S. National Science Foundation (NSF) (P.A.G., 1728239), an NSF Graduate Research Fellowship (B.G., 1450681), the U.S. National Heart, Lung, and Blood Institute (NHLBI) of the National Institutes of Health (NIH) via F31 NRSA Fellowship (S.J.P., HL134295), the NIH Director's New Innovator Award (K.R.S., NHLBI, DP2HL137188), the John H. Tietze Foundation (K.R.S.), NIH National Institute of Biomedical Imaging and Bioengineering (NIBIB) Cardiovascular Training Grant (D.C.C., T32EB001650); NIH National Institute of General Medical Sciences (NIGMS) Molecular Medicine Training Grant (C.L.F., T32GM095421); Office of the Director of the National Institutes of Health Early Independence Award (A.R., DP5OD019876), and a training fellowship from the Gulf Coast Consortia on the NSF IGERT: Neuroengineering from Cells to Systems (D.W.S., 1250104). The content is solely the responsibility of the authors and does not necessarily represent the official views of any of the funding agencies. **Author contributions:** B.G. and J.S.M. conceived and initiated the project. All authors contributed to experimental design, planning, and execution; data analysis; and manuscript writing. B.G., S.J.P., D.W.S., J.E.R., J.D.L-R., and J.S.M. developed designs and algorithms. A.R., P.G., K.R.S., and J.S.M. supervised the project. **Competing interests:** J.S.M. and B.G. are cofounders of and hold an equity stake in the startup company Volumetric, Inc. J.E.R. and J.D.L-R. are cofounders and hold an equity stake in Nervous System, Inc., a design studio that works at the intersection of science, art, and technology. B.G., A.H.T., and J.S.M. are listed as co-inventors on pending U.S. patent application 15/709,392. D.C.C., K.R.S., B.G., and J.S.M. are listed as co-inventors on pending U.S. patent application 62/746,106. The remaining coauthors declare no competing interests. **Data and materials availability:** Data, SLATE design files, and hydrogel STL design files are available in Zenodo (*39*). HARVEY (*40*) is a closed-source code that is available under a research license from Duke University. Research licenses can be applied for at the Duke University Office of License and Ventures. Plasmids pTRIP.Alb.IVSb.IRES.tagRFP-DEST and pTRIP.Alb.Fluc.ires.TagRFP.NLS-IPS (*41*) were provided by C. Rice, The Rockefeller University, under a uniform biological material transfer agreement with The Rockefeller University.

SUPPLEMENTARY MATERIALS

science.sciencemag.org/content/364/6439/458/suppl/DC1
Materials and Methods
Figs. S1 to S15
Table S1
References (*42*–*68*)
Movies S1 to S5

6 November 2018; accepted 9 April 2019
10.1126/science.aav9750

Multivascular networks and functional intravascular topologies within biocompatible hydrogels

Bagrat Grigoryan, Samantha J. Paulsen, Daniel C. Corbett, Daniel W. Sazer, Chelsea L. Fortin, Alexander J. Zaita, Paul T. Greenfield, Nicholas J. Calafat, John P. Gounley, Anderson H. Ta, Fredrik Johansson, Amanda Randles, Jessica E. Rosenkrantz, Jesse D. Louis-Rosenberg, Peter A. Galie, Kelly R. Stevens and Jordan S. Miller

Science **364** (6439), 458-464.
DOI: 10.1126/science.aav9750

Routes to independent vessel networks

In air-breathing vertebrates, the circulatory and pulmonary systems contain separate networks of channels that intertwine but do not intersect with each other. Recreating such structures within cell-compatible materials has been a major challenge; even a single vasculature system can be a burden to create. Grigoryan *et al.* show that natural and synthetic food dyes can be used as photoabsorbers that enable stereolithographic production of hydrogels containing intricate and functional vascular architectures. Using this approach, they demonstrate functional vascular topologies for studies of fluid mixers, valves, intervascular transport, nutrient delivery, and host engraftment.

Science, this issue p. 458